First-principles calculations of equilibrium nitrogen isotope fractionations among aqueous ammonium, silicate minerals and salts

Yonghui Li[1,2], Long Li[2*], Zhongqing Wu[1,3*]

1 Laboratory of Seismology and Physics of Earth's Interior, School of Earth and Space, University of Science and Technology of China, Hefei, Anhui 230026, China

2 Department of Earth and Atmospheric Sciences, University of Alberta, Edmonton, Alberta, T6G 2E3, Canada

3 CAS Center for Excellence in Comparative Planetology, University of Science and Technology of China, Hefei, Anhui 230026, China

*Corresponding author: LL (long4@ualberta.ca); ZW (wuzq10@ustc.edu.cn)

ABSTRACT:

Nitrogen isotopes are a robust tool to study geological nitrogen cycle between Earth's reservoirs. However, the application of nitrogen isotope system to understanding geological processes has been limited by the lack of constraints on equilibrium isotope fractionation factors between mineral and fluid and between mineral pairs. Here, we use first-principles methods to calculate the nitrogen isotope fractionations among aqueous ammonium, ammonium- and/or nitrate-bearing salts, and ammonium-bearing silicate minerals that commonly occur in Earth's lithosphere. Our results show a first-order, large nitrogen isotope fractionations between the nitrate group and the ammonium group, with ^{15}N being more enriched in the nitrate group. In detail, the nitrogen isotope fractionations among nitrate group minerals ($NaNO_3$, KNO_3, $Ba(NO_3)_2$, NH_4NO_3) are very small. The nitrogen isotope fractionations are also small among the ammonium group (e.g., aqueous ammonium, ammonium salts, phyllosilicate, and tectosilicate minerals) except inosilicate minerals (e.g., diopside and jadeite), which are however significantly more enriched in ^{15}N than the other ammonium-bearing minerals. These results suggest that nitrogen isotopes may serve as a robust geothermometer only when the rock contains coexisting ammonium and nitrate minerals, or contain diopside and/or jadeite together with other ammonium-bearing silicate minerals. Given that common silicate minerals in crustal rocks (clays, micas, feldspars) do not significantly discriminate nitrogen isotopes, nitrogen isotopes can thus be used as a sensitive tool to trace material source and infer geochemical processes that may cause isotope disequilibrium, such as metamorphic devolatilization, hydrothermal

alteration, crust-mantle interaction. Our results also demonstrate that authigenic clay minerals can inherit the nitrogen isotopic signature of organic matter and aqueous ammonium and thus can serve as an environmental proxy. However, it is crucial to distinguish detrital minerals from authigenic minerals in sediments when reconstruct marine and lacustrine environments in the deep time (Archean and Proterozoic).

1. Introduction

Nitrogen is one of the few elements occurring in all Earth's reservoirs from the surface (e.g., the atmosphere, hydrosphere/biosphere, and crust) to the interior (e.g., the mantle). The geological nitrogen cycle could have played an important role in the long-term evolution of physiochemical properties of Earth's subsystems, but is still poorly understood (e.g., Marty and Dauphas, 2003; Cartigny and Marty, 2013).

In the lithosphere, nitrogen mainly occurs as ammonium- and/or nitrate-bearing salts produced in sedimentary and hydrothermal environments, and as ammonium in crystal lattice of silicate minerals by replacing potassium (Honma and Itihara, 1981), sodium, and calcium (Watenphul et al., 2010). To a less extent, nitrogen may occur in silicate melts and hydrothermal fluids in a variety of species, including nitrate, N_2, ammonium/ammonia, and many others such as CN- or N-O (e.g., Roskosz et al., 2006; Li et al., 2013; Li and Keppler, 2014; Mikhail et al., 2014, 2017; Dalou et al., 2019a).

59   Previous theoretical (e.g., Urey, 1947; Scalan, 1958; Hanschmann, 1981; Petts et al.,

60   2014) and experimental studies (e.g., Haendel et al., 1986; Li et al., 2009, 2012; Li et

61   al, 2016; Deng et al., 2018) have demonstrated large isotope fractionations between

62   species involved in hydrothermal fluid and melt. Consequently, nitrogen isotopes have

63   been considered to be a robust tool to trace geological nitrogen cycle (e.g., Haendel et

64   al., 1986; Bebout and Fogel, 1992; Bebout, 1997; Bebout et al., 1999, 2013; Sano et al.,

65   1998; Mingram and Bräuer, 2001; Busigny et al., 2003a, 2013; Li and Bebout, 2005;

66   Halama et al., 2010; Plessen et al., 2010; Li et al., 2014; Li et al., 2019a). However, the

67   nitrogen isotope fractionation factors between minerals are mostly lacking despite of

68   some recent efforts (e.g., Sadofsky and Bebout, 2000; Bebout et al., 2016), making it

69   difficult to assess isotope equilibrium or disequilibrium between coexisting minerals in

70   a rock, or between minerals and fluid in a hydrothermal system, which is the key

71   information for understanding the evolution history of a geological system.

72   Recently, accurate calculations based on density functional theory (DFT), a

73   computational quantum mechanical modelling method for investigating the electronic

74   structure of many-body system, have been successfully applied to predict equilibrium

75   isotope fractionation factors among minerals for a number of isotope systems for the

76   excellent performance of DFT on prediction of crystal volumes and vibrational

77   frequencies (Rustad and Yin, 2009; Young et al., 2009; Liu et al., 2011; Schauble, 2011;

78   Dauphas et al., 2012; Huang et al., 2013; Wang et al., 2017; Li et al., 2019b, c). Here,

79   we applied DFT-based calculations to determine the equilibrium nitrogen isotope

80   fractionation factors among a variety of nitrogen-bearing minerals commonly occurring

81　in Earth's lithosphere, including ammonium-bearing silicates (e.g., albite,

82　buddingtonite, microcline, muscovite, tobelite, phlogopite, biotite, diopside, jadeite)

83　and ammonium- and/or nitrate-bearing salts (e.g., NH_4Cl, $(NH_4)_2SO_4$, NH_4NO_3, KNO_3,

84　$NaNO_3$, $Ba(NO_3)_2$). Besides, a synthetic aluminosilicate zeolite Linde J

85　$(Si_2Al_2O_8(NH_4)_2H_2O)$ was also calculated in reference for natural ammonium-bearing

86　clay minerals, whose structures are largely unknown and thus are not amenable to

87　theoretical calculations. In addition, we also simulated the structures of ammonium in

88　aqueous solution using the Car-Parrinello molecular dynamics (CPMD) (Car and

89　Parrinello, 1985) and predicted the equilibrium N isotope fractionation factors between

90　minerals/salts and aqueous solution. This study aims to provide essential data for

91　nitrogen isotope applications to broad geological settings from low-temperature

92　sedimentation process to high-temperature igneous and metamorphic processes.

93

94　**2. Methods**

95　*2.1 The reduced partition function ratio and equilibrium isotope fractionation factor*

96　　The reduced partition function ratio (RPFR) of element X in phase A, which is

97　denoted as β_A, describes the equilibrium isotope fractionation factor of element X

98　between phase A and ideal gas of X atoms. Under the harmonic approximation,

99　according to quantum mechanics and statistical physics, following Bigeleisen and

100　Mayer (1947) and Urey (1947), the β_A can be written as:

101
$$^{15}\beta_A = \prod_{i=1}^{3N-3} \left(\frac{u_i^*}{u_i} \frac{e^{-\frac{1}{2}u_i^*}}{1-e^{-\frac{1}{2}u_i^*}} \frac{1-e^{-\frac{1}{2}u_i}}{e^{-\frac{1}{2}u_i}} \right) , \tag{1}$$

102　where $u_i = hv_i/kT$; v_i is the i-th vibrational frequency; h and k are the Planck and

103 Boltzmann constants, respectively; the asterisk superscript refers to the heavy isotope;

104 N is the number of atoms in the crystal which has $3N$-3 non-zero vibrational modes.

105 Based on equation 1, we can also obtain the RPFR in phase B, which is denoted as β_B.

106 The equilibrium isotope fractionation factor between phase A and phase B, which is

107 denoted as α_{A-B}, can be defined as:

108
$$10^3 \ln \alpha_{A\text{-}B} = 10^3 (\ln \beta_A - \ln \beta_B) \tag{2}$$

109

110 ### 2.2 The first-principles calculations

111 Optimization of mineral crystal structures were performed by using the Quantum

112 Espresso (QE) software (http://www.quantum-espresso.org) which was built on DFT,

113 plane wave and pseudopotential method (Giannozzi et al., 2009). The Generalised-

114 Gradient Approximation (GGA) (Perdew et al., 1996) with Perdew-Burke-Ernzerhof

115 (PBE) exchange correlation function were applied for the calculations. The detailed

116 pseudopotentials of H, N, O, Na, Mg, Al, Si, S, Cl, K, Ca, Fe and Ba used in our

117 calculations were listed in the supplementary data Table S1. For structure optimization

118 of minerals, the cutoff of the plane wave energy was set to 70 Ry, while the convergence

119 threshold on forces for ionic minimization and energy for self-consistency were 10^{-4}

120 Ry/Bohr and 10^{-8} Ry respectively. The k mesh sampling (Table S2) used in vc-relax was

121 based on the crystal structures in Fig. 1.

122 To examine the nitrogen isotopic behavior of NH_4^+ in aqueous solution, we

123 performed the CPMD modeling on a cubic cell of $NH_4Cl(H_2O)_{32}$ that contains one NH_4^+

124 and 32 H_2O molecules with one Cl^- being added to retain a charge balance. It has been

125 demonstrated that ammonium can be fully hydrated by 32 H_2O molecules, which can

126 thus represent a solution environment (Li et al., 2021). Variable-cell CPMD module in

127 QE was used for the calculations. The Nosé-Hoover thermostats method (Nosé, 1984;

128 Hoover, 1985) was used to maintained the system temperature at 300 K and the standard

129 Verlet algorithm (Parrinello and Rahman, 1980, 1981) was used to adjust cell volume

130 to retain the pressure at 0.00 Gpa. The convergence threshold of total energy and force

131 in the CPMD simulation were near 0.5×10^{-8} Ry and 0.5×10^{-5} Ry/Bohr, respectively. The

132 time step was ~0.12 fs and the total simulation time was up to ~18.14 ps (150000 steps).

133 The detailed explanations of these parameters are given in the webpage:

134 http://www.quantum-espresso.org/resources/users-manual/input-data-description.

135 The vibrational frequencies on gamma point were obtained by the open source

136 code PHONOPY (Togo and Tanaka, 2015) which was based on finite displacement

137 method. The structure optimization and vibrational frequency calculations of biotite

138 were achieved by GGA+U method with a self-consistent Hubbard_U value of 3.50 eV

139 (Cococcioni and Gironcoli, 2005).

140

141 *2.3 Initial crystal structures*

142 The initial crystal structures for our calculations were either from the American

143 Mineralogist Crystal Structure Database (AMCSD), e.g., for jadeite, diopside,

144 phlogopite, biotite, albite, microcline, buddingtonite, tobelite, KNO_3, and NH_4NO_3

145 (phase V), or from the Inorganic Crystal Structure Database (ICSD), e.g., for Linde J,

146 $NaNO_3$, NH_4Cl, and $(NH_4)_2SO_4$.

147   For the calculations of silicate minerals, since NH_4^+ concentration varies

148   significantly from major component (e.g., in buddingtonite, tobelite, Linde J) to trace

149   elements (e.g., in K-feldspar, plagioclase, muscovite, biotite, phlogopite,

150   clinopyroxene), we used a doping method for trace NH_4^+-bearing minerals. For

151   feldspars and muscovite, we doped K^+ or Na^+ to the NH_4^+ cluster in a supercell of

152   buddingtonite and tobelite, respectively, to obtain different NH_4^+ occupation ratio,

153   which is expressed as $NH_4^+/(NH_4^+ + K^+$ or $Na^+)$ occupation in molar ratio. For example,

154   in the $2 \times 1 \times 2$ supercell of buddingtonite, we replaced 15 NH_4^+ by 15 K^+ to generate an

155   initial crystal structure of microcline with the NH_4^+ occupation ratio of 1/16. The crystal

156   structure of NH_4^+-doped jadeite, phlogopite, and biotite were constructed by replacing

157   K^+ or Na^+ by the NH_4^+ cluster. For NH_4^+-bearing diopside, Watenphul et al. (2010)

158   found that NH_4^+ can replace Ca^{2+} in M2 site while Mg^{2+} in M1 site is replaced by M^{3+}

159   (e.g., Al^{3+} or Cr^{3+}). Accordingly, we substituted one set of Ca^{2+} and Mg^{2+} by one set of

160   NH_4^+ and Al^{3+} in the $1 \times 1 \times 2$ supercell of diopside to generate the initial crystal structure

161   of NH_4^+-bearing diopside with an NH_4^+ occupation ratio of 1/8. While several

162   nonequivalent substituted configurations were yielded, we chose the one with the

163   lowest total energy for our calculation.

164   The Si-Al occupation models in buddingtonite and tobelite crystals were the same

165   as our previous calculations for K isotope fractionations in microcline and muscovite

166   (Li et al., 2019b, c).

167

3. Results

3.1. Crystal structure and average bond length

170   The calculated structures of minerals and $NH_4Cl(H_2O)_{32}$ are illustrated in Fig. 1.

171 In the optimized buddingtonite, the b axis is not normal to the a and c axes (α and γ are

172 not 90.0° in SI - Table S3). This can be attributed to the specific Si-Al occupation, which

173 will break the symmetry of the crystal structures of buddingtonite, resulting in shift of

174 the crystal structure toward that of microcline. Similar deformation of crystal structure

175 from tobelite to muscovite was also observed during the calculations. Compared with

176 available experimental volume measurements on buddingtonite, tobelite, Linde J,

177 NH_4Cl, $(NH_4)SO_4$, $NaNO_3$, KNO_3, $Ba(NO_3)_2$, NH_4NO_3-V, and $NH_4Cl(H_2O)_{32}$

178 (Vainshtein, 1956; Amoros et al., 1962; Schlemper and Hamilton, 1966; Cherin et al.,

179 1967; Nimmo and Lucas, 1973; Nowotny and Heger, 1983; Mookherjee et al., 2004;

180 Broach and Kirchner, 2011; Mesto et al., 2012; Stefan-Kharicha et al., 2018), our

181 calculated volumes are 3-4% larger. This is consistent with previous first-principles

182 studies (Li et al., 2019c; Schauble, 2011; Wentzcovitch et al., 2010) showing that the

183 GGA function tends to slightly overestimate the volumes, in contrast to the other

184 commonly used Local Density Approximation (LDA) function which tends to slightly

185 underestimate the volumes. As a result, the GGA function tends to give underestimated

186 RPFR values, whereas the LDA tends to give overestimate RPFR values. Nevertheless,

187 the systematic offset associated with individual function (either GGA or LDA) can be

188 canceled out during the calculation of equilibrium isotope fractionation factors. As a

189 result, the GGA and LDA methods should give similar $10^3ln\alpha$ results for mineral pairs,

190 as demonstrated by Huang et al. (2013).

191   The calculated average lengths (Table 1) of the N-H bonds in minerals and salts

192 show relatively small variations, from the smallest length of 1.0203Å in jadeite to the

193 largest length of 1.0420 Å in $(NH_4)_2SO_4$. The calculated average lengths of the N-O

194 bonds in the nitrate salts ($NaNO_3$, KNO_3, $Ba(NO_3)_2$, NH_4NO_3) cluster in a very limited

195 range from 1.2733Å ($NaNO_3$) to 1.2761Å (KNO_3) (see Table 1).

196   To describe the structure of NH_4^+ in aqueous solution, we simulated the density

197 variation of H as a function of its distance from N, which can be expressed by the radial

198 distribution function (RDF) (Liu et al., 2018):

199 $$g_{N-H}(\mathrm{r}) = \frac{n}{\rho n_N n_H} \left(\sum_{i=1}^{n_N} \sum_{j=1}^{n_H} \left(\vec{r} - \vec{R}_i^N + \vec{R}_j^H \right) \right) \tag{3}$$

200 in which n denotes the number of atoms; $\rho = n/V$; V is the volume of the system; $\vec{R}$ is

201 the coordinates of atoms. The $g_{N-H}(\mathrm{r})$ value gives the probability of finding a H atom

202 at a distance of r away from a N atom. We yielded a strong peak around 1.046 Å (Fig.

203 2), indicating the N-H bond length of the NH_4^+ cluster. Integration of the peak in Fig.

204 2A gives the number of the nearest neighbor atoms, or the coordination number (CN).

205   We extracted 20 snapshots from the simulation of $NH_4Cl(H_2O)_{32}$ trajectories after

206 equilibrium, with volumes close to 1055.91 $Å^3$ (to ensure the pressure is near 0.0 Gpa),

207 to perform ionic relaxation, full vibrational frequency calculation and $10^3 ln\beta$ prediction

208 (Table S4 & S6). The N-H bond lengths of these 20 snapshots range from 1.0441 Å to

209 1.0491 Å with an average of 1.0457 Å (Table S4), which is used to represent the N-H

210 bond length of aqueous ammonium. Accordingly, the bond length of aqueous

211 ammonium is larger than the ammonium in all minerals and salts.

212

3.2 Vibrational frequencies

To validate our calculation results, we compared the yielded vibrational frequencies of the NH_4^+ and NO_3^- clusters in a variety of minerals with experimental results. A free NH_4^+ cluster is in tetrahedral symmetry (T_d) and has four normal modes of vibrations (Herzberg. 1955), i.e., A_1 (v_1), E (v_2) and $2 \times T_2$ (v_3 and v_4). Their vibration frequencies may be different in different minerals. Compared with available experimental data measured by Raman or IR analyses (see summary in Table S5), our calculated vibrational frequencies of $(NH_4)_2SO_4$, buddingtonite, tobelite, NH_4Cl and phlogopite-(NH_4) show a high consistency (Table S5; Fig. 3), which demonstrates that GGA is a good exchange-correlation function for predicting vibrational frequencies of nitrogen bonds.

3.3. The predicted $^{15}\beta$ values and calculation uncertainty

The calculated $10^3 ln\beta$ values of the studied minerals (some with variable NH_4^+ concentration) at selected temperatures are listed in Table S6. The $10^3 ln\beta$ data are fitted by a general polynomial equation:

$$10^3 ln\beta = C_0 + \frac{C_1}{10} \times x - \frac{C_2}{10^2} \times x^2 + \frac{C_3}{10^3} \times x^3 - \frac{C_4}{10^4} \times x^4 + \frac{C_5}{10^5} \times x^5 - \frac{C_6}{10^6} \times x^6 \quad (4)$$

in which $x = 10^6/T^2$; $C_0 - C_6$ are constant. The yielded $C_0 - C_6$ values are listed in Table 1. The temperature-dependent $10^3 ln\beta$ values are illustrated in Fig. 4.

The uncertainty (at 95% confidence level) of $10^3 ln\beta$ is 0.9% of their corresponding values. This is estimated based on the uncertainty analysis by Méheut et al. (2009), which showed that the uncertainty of the predicted β is correlated with the scale factor

235 (slope) of the predicted vibrational frequencies (1.009 in our calculations).

236 Overall, our results show that the nitrate group minerals are more enriched in ^{15}N

237 than are the ammonium group minerals (Fig. 4A). Interestingly, the variability of $10^3\ln\beta$

238 in the nitrate group is very small, with a difference of 2.1‰ at 300 K (Fig. 4B) and 0.9‰

239 at 575 K between the most ^{15}N enriched mineral ($NaNO_3$) and the most ^{15}N depleted

240 mineral (NH_4NO_3). In the ammonium group minerals, the variation of $10^3\ln\beta$ is much

241 larger – ^{15}N enrichment is highest in jadeite, and progressively decreases along the

242 order of diopside, albite, microcline, buddingtonite, phlogopite, biotite, NH_4NO_3,

243 muscovite, tobelite, clay, $(NH_4)_2SO_4$, and NH_4Cl. In particular, clinopyroxene minerals

244 (jadeite and diopside) show much higher $10^3\ln\beta$ values than the other minerals in the

245 ammonium group, e.g., jadeite has $10^3\ln\beta$ higher than mica minerals for ~ 5‰ at 575

246 K and ~3‰ at 775 K (Fig. 4C; Table S6).

247 The $10^3\ln\beta$ values calculated from the 20 snapshots of $NH_4Cl(H_2O)_{32}$ range from

248 91.5‰ to 92.6‰ at 300 K. Again, we use the average $10^3\ln\beta$ value of these 20 snapshots

249 to represent the $10^3\ln\beta$ value of aqueous ammonium, which is 92.0‰ at 300 K. This

250 value is smaller than those of the minerals and salts examined in this study (92.3-

251 109.4‰; Table S6).

252

253 **4. Discussion**

254 *4.1. The control of bond strength on ^{15}N enrichment*

255 Our calculation results show clear control of bond strength on the ^{15}N enrichment

256 in minerals. For example, nitrate minerals all have larger $10^3\ln\beta$ values than ammonium

257 minerals. This is consistent with more ^{15}N enrichment in higher valence state (Schauble,

258 2004). The control of bond strength on ^{15}N enrichment among the ammonium group

259 minerals is reflected by the negative correlation between $10^3\ln\beta$ values and average

260 bond length (Fig. 5), which is consistent with our previous study on K isotope

261 fractionations in K-bearing minerals (Li et al., 2019c).

262

263 *4.2. Concentration effect on N isotope fractionation*

264 Ammonium in common silicate minerals in natural rocks (e.g., micas, feldspars

265 and clinopyroxene) is at trace level (from a few to thousands of ppm; e.g., Sadofsky

266 and Bebout, 2000; Busigny et al., 2003b, 2004; Li et al., 2014). In a previous study on

267 K isotope fractionations, we have observed that, when K^+ concentration in alkali

268 feldspars decreases, the large radius of K^+ must be compressed, which results in

269 significant change in the average K-O bond length and consequent change in isotope

270 fractionations (a variation of $10^3\ln\beta$ for ~0.2‰ even at 700 ºC; Li et al., 2019b). Since

271 ammonium mostly occupies the K^+ position in mineral lattice (Honma and Itihara,

272 1981), we also examined whether decreased NH_4^+ concentrations would affect the

273 magnitude of nitrogen isotope fractionation. Surprisingly, our calculations for the

274 buddingtonite-microcline series with NH_4^+ occupation ratio varying from 4/4 to 1/16

275 (equivalent to 2780 ppm NH_4^+ in K-feldspar) only gave a $10^3\ln\beta$ difference of ~ 0.18‰

276 at 300 ºC and ~ 0.05‰ at 700 ºC (Table S6). Similar results are observed from all the

277 calculation practices on some other minerals (i.e., the tobelite-muscovite series,

278 phlogopite, biotite, and albite; Table S6). These values are insignificant compared with

279 the analytical error of 0.2‰ (e.g., Bebout et al., 2007) for nitrogen isotope compositions

280 of silicate. Overall, in silicate minerals, the concentration effect on nitrogen isotope

281 fractionations is much weaker than that on K isotopes (Li et al., 2019b) and Ca isotopes

282 (Wang et al., 2017). This may be mainly attributed to the flexibility of the NH_4^+ cluster,

283 which can deform its shape to fit in different crystal structure. For example, in the

284 buddingtonite-microcline series, when the NH_4^+ occupation ratio increases from 1/16,

285 1/4, to 4/4, the NH_4^+ tetrahedron is more and more deformed via changing its four N-H

286 bond lengths and six N-H bond angles, which can be quantified by the increase in the

287 variances (defined by Equation 4 below) of the four N-H bond lengths and the six N-H

288 bond angles of the NH_4^+ tetrahedron:

289
$$s_{ang \ or \ len} = \frac{1}{n-1}\sum_{i=1}^{n}(x_i - \bar{x})^2 \quad\quad (5)$$

290 where ang and len denote bond angle and bond length, respectively; x_i is the i-th

291 bond length or angle; $\bar{x}$ denotes the average bond length or angle; n is the number of

292 bonds ($n = 4$) or angles ($n = 6$) in NH_4^+. Interestingly, despite of the large changes in

293 the N-H bond lengths and N-H bond angles (Table S7), the average N-H bond length is

294 able to remain nearly constant (Table 1). Consequently, the change in ammonium

295 concentration in minerals does not affect nitrogen isotope fractionation significantly.

296   Because the concentration effect on nitrogen isotope fractionation is very small in

297 silicate minerals, and the lowest NH_4^+ occupation ratio (i.e., 1/16 in the buddingtonite-

298 microcline series; equivalent to 2780 ppm NH_4^+ in microcline) overlaps the upper end

299 of the NH_4^+ concentration range of natural minerals (up to > 3000 ppm; e.g., Busigny

300 et al., 2003b, 2004), our calculation results can be comfortably applied to natural

301 systems. To apply to field case studies, we recommend using the data calculated from

302 NH_4^+ or NO_3^- occupation ratio of 1:1 for the minerals that have high N contents (e.g.,

303 ammonium salts, nitrate salts, buddingtonite and tobelite). For the silicate minerals

304 containing trace amounts of nitrogen, we recommend using the results from NH_4^+

305 occupation ratios of 1/16 (for microcline, and likely other K-feldspar as well) or 1/8

306 (for muscovite, biotite, phlogopite, albite, diopside, and jadeite). For clay minerals, a

307 supercell contains a large number of atoms (Table S2), which makes the calculation

308 very difficult. Consequently, we only calculated an occupation ratio of 1/1 for Linde J.

309 The results should not deviate much from the real fractionation of clay minerals, given

310 that the concentration effect on nitrogen isotope fractionation is very weak.

311

4.3. Nitrogen isotope fractionations between silicate minerals

313 The nitrogen isotope fractionations between individual minerals relative to

314 aqueous NH_4^+ were derived from their $10^3 \ln\beta$ values (Table S6) according to Equation

315 2. Their general description equations are listed in Table 2 and plotted in Fig. 6. The

316 results show resolvable nitrogen isotope fractionations between inosilicate (e.g., the

317 clinopyroxene group), tectosilicate (e.g., the feldspar group), and phyllosilicate

318 minerals (e.g., the mica/clay group). This reflects a strong control of silicate structure

319 on nitrogen isotope fractionation despite the strong adjustable capability of ammonium

320 in silicate structures that can alleviate nitrogen isotope discrimination. Another factor

321 that can affect nitrogen isotope fractionation is the relative radius difference between

322 NH_4^+ and its replaced cation (e.g., K^+, Na^+ or Ca^{2+}). This has been observed in our

15

323 previous study for K isotopes (Li et al., 2019b). The ionic radius of NH_4^+ (~1.670 Å) is

324 similar to that of Rb^+ (1.660 Å) but longer than that of K^+ (1.520 Å) and much longer

325 than Na^+ (1.160 Å) and Ca^{2+} (1.140 Å) (Shannon,1976; Honma and Itihara, 1981; Sidey,

326 2016). As a result, the radius difference between NH_4^+ and Na^+ (0.51 Å) is larger than

327 that between NH_4^+ and K^+ (0.15 Å), which induces greater ^{15}N enrichment in albite than

328 the buddingtonite-microcline series (Table S6, Fig 4, 6).

329

330 ### 4.4. Nitrogen isotope fractionations between minerals and aqueous ammonium

331 The $10^3\ln\alpha$ values between minerals and aqueous ammonium (represented by

332 $NH_4Cl(H_2O)_{32}$) are listed in Table 2 and plotted in Fig. 6. Our calculation shows that,

333 compared with silicate minerals and salts, aqueous ammonium is more depleted in ^{15}N

334 (Fig. 6). This is consistent with the fact that ammonium is more strongly bound in solid

335 phase than in aqueous phase. The magnitude of nitrogen isotope fractionation between

336 minerals and aqueous ammonium varies significantly, depending on the nitrogen

337 speciation (ammonium or nitrate) and mineral structures (e.g., phyllosilicate,

338 tectosilicate, inosilicate). In general, nitrate minerals show large ^{15}N enrichment relative

339 to aqueous ammonium, which can be attributed to their high valence state (see

340 discussion above). Among ammonium-bearing minerals, inosilicate minerals show the

341 greatest magnitude of nitrogen isotope fractionation relative to aqueous ammonium,

342 followed by tectosilicate minerals, phyllosilicate minerals and salts (Figs. 3-4). These

343 new data, together with the recent constraints on nitrogen isotope fractionations

344 between a variety of nitrogen species in hydrothermal fluid (Li et al., 2021), provide

16

345 new opportunities for petrological and environmental studies.

346

5. Applications to petrology, geothermometry and source tracing

5.1. Equilibrium, disequilibrium and geothermometry for igneous and metamorphic rocks

Sadofsky and Bebout (2000) examined the nitrogen isotope compositions of muscovite and coexisting biotite in amphibolite-facies metapelites in the New England Appalachians. They found that the less altered muscovite and biotite have mean $\Delta^{15}N_{biotite-muscovite}$ of ~0.1‰ (Sadofsky and Bebout, 2000). This observation is consistent with our calculated results that the nitrogen isotope fractionations between biotite and muscovite is <0.2‰ at temperatures higher than 500ºC (Table S6; Fig. 6B).

Our calculated results also show that the nitrogen isotope fractionations between feldspars and micas are very small (e.g., <1.1‰ at 300 ºC and < 0.5‰ at 700 ºC between albite and muscovite; Fig. 6B; Table S6). Because micas and feldspars are the most common ammonium-bearing minerals in intermediate and felsic rocks, the nitrogen isotope fractionations between coexisting minerals in these rocks are too small to allow nitrogen isotopes to serve as a robust geothermometer. However, this feature facilitates nitrogen isotopes to serve as a sensitive tool to probe processes that may cause nitrogen isotope disequilibration between these minerals, such as fluid alteration, abiotic nitrogen reduction, nitrogen devolatilization, crustal-mantle interaction. For example, Li et al. (2014) observed extreme ^{15}N depletions in biotite (up to 20‰ lower than the values of white micas) in the ultrahigh-pressure (UHP) metamorphic rocks in the Sulu

orogen in eastern China. This indicates an obvious nitrogen isotope disequilibrium between the biotite and white micas, which helped to identify an abiotic nitrogen reduction process during the hydrothermal alteration of the protolith of these UHP metamorphic rocks (Li et al., 2014).

In mafic and ultramafic rocks, clinopyroxene minerals commonly occur, sometimes coexisting with micas (e.g., phlogopite or biotite) and/or feldspars. In this case, the large isotope fractionation factors between clinopyroxene mineral and feldspar or mica (Fig. 6B) can help to examine the isotope equilibration or disequilibration between these minerals and, if at equilibrium, to determine the formation temperature of these minerals.

5.2. Nitrogen isotopic inheritance in clay and its application as an environmental proxy

Phyllosilicate minerals such as clay are widely developed on Earth's surface, from soil development on land to sediment diagenesis and hydrothermal alteration of oceanic crust on seafloor. Therefore, low-temperature mineralization of phyllosilicate minerals plays a key role in the geological nitrogen cycle by fixing ammonium from the hydrosphere/biosphere into the lithosphere.

The nitrogen isotopic transfer along this geological nitrogen recycling pathway is a crucial parameter to model the isotopic evolution of involved Earth's reservoirs. Our results show that, although ^{15}N is more enriched in clay than aqueous ammonium, the magnitude is small (e.g., 1.6‰ at 300 K; Table S6). This is consistent with a previous

389   laboratory study (Karamanos and Rennie, 1978) showing that ^{15}N is more enriched in

390   clay (with a slightly higher value of ~3‰) during ammonium solution-clay exchange

391   experiments. Interestingly, ammonium produced by organic degradation in water

392   column and early diagenesis is associated with a nitrogen isotope fractionation of -1.5‰

393   (Freudenthal et al., 2001). As a combined effect, authigenic clay in sediments should

394   have $\delta^{15}N$ value nearly identical to that of organic matter. Therefore, our new data well

395   explain the widely observed phenomenon that authigenic clay can inherit the $\delta^{15}N$ of

396   organic matter (e.g., Williams et al., 1995) despite nitrogen isotopes fractionation

397   occurs in several steps along this nitrogen transfer pathway. Similarly, during the low-

398   temperature alteration of oceanic crust, clay minerals can also be produced as a

399   common secondary mineral. If ammonium is available in seawater, it can be assimilated

400   into clay minerals without significant isotopic shift from the seawater signature. This

401   has been proved by nitrogen isotopic examinations of oceanic crust samples drilled

402   from worldwide oceans (e.g., Busigny et al., 2005; Li et al., 2007, Bebout et al., 2018).

403   Accordingly, our new data demonstrate that authigenic clay in sediments and oceanic

404   crust can reliably record the nitrogen isotopic signature of ammonium in these settings,

405   and thus serve as a proxy to reconstruct the nitrogen isotopic signature of paleo-

406   seawater, diagenetic fluid, or hydrothermal fluid. However, when use seafloor sediment

407   and/or oceanic crust to study the nitrogen signature of paleo-oceans, caution must be

408   taken to ensure the nitrogen-bearing phases were authigenic, which may not be

409   necessarily true. For example, Pinti et al. (2009) examined the nitrogen in cherts from

410   the Archean Pilbara Craton and found two possible nitrogen-bearing phases coexisting

411 in some samples, i.e., illite and feldspar. However, the $\delta^{15}N$ values of these two phases

412 display a $\delta^{15}N$ difference of more than 10‰ (Pinti et al., 2009). Our new data indicates

413 obvious nitrogen isotope disequilibrium between these two phases in the Archean cherts.

414 This suggests that at least one of them was not authigenic but either detrital or

415 introduced by later tectonic activities.

416

417 **5. Conclusions**

418   Via first principle calculations, we obtained the equilibrium isotope fractionation

419 factors for a variety of minerals, including ammonium- and nitrate-bearing salts and

420 ammonium-bearing silicate minerals, as well as aqueous ammonium. We found a large

421 isotope fractionation between nitrate group minerals and ammonium group minerals

422 with ^{15}N is more enriched in nitrate. In ammonium group minerals, inosilicate minerals

423 (e.g., clinopyroxene) are most enriched in ^{15}N, followed by tectosilicate (e.g., feldspars),

424 phyllosilicate (e.g., micas and clays), and ammonium salts. The nitrogen isotope

425 fractionation between mica minerals, clays and ammonium salts are very small (<1‰)

426 at high temperatures. We suggest that only an equilibrium temperature derived from

427 rocks that contain clinopyroxene minerals together with feldspar or mica minerals are

428 meaningful. The small magnitudes of nitrogen isotope fractionation between feldspars

429 and mica minerals, which commonly coexist in crustal rocks, are too small to be used

430 for geothermometer. However, these small isotope fractionations enable nitrogen

431 isotopes to be a sensitive tool to trace material course and detect geological processes

432 superimposed on the common equilibrium processes in high-temperature igneous and

metamorphic events. Our data also demonstrate that authigenic clay is a robust proxy

to reconstruct the nitrogen isotopic signatures of the aqueous environment where it was

formed.

References

Amoros J L., Arrese F., Canut M. (1962) The crystal structure of the low-temperature phase of NH_4NO_3(V) at -150 deg C. *Zeitschrift fur Kristallographie* **117**, 92-107.

Bebout, G.E. (1997) Nitrogen isotope tracers of high-temperature fluid-rock interactions: case study of the Catalina Schist, California. *Earth Planet. Sci. Lett.* **151**, 77-90.

Bebout, G.E. and Fogel, M.L. (1992) Nitrogen-isotope compositions of metasedimentary rocks in the Catalina Schist, California: implications for metamorphic devolatilization history. *Geochim. Cosmochim. Acta* **56**, 2839–2849.

Bebout, G.E., Cooper, D.C., Bradley, A.D., Sadofsky, S.J. (1999) Nitrogen-isotope record of fluid–rock interactions in the Skiddaw Aureole and granite, English Lake District. *Am. Mineral.* **84**, 1495–1505.

Bebout, G.E., Idleman, B.D., Li, L., Hikert, A. (2007) Isotope-ratio-monitoring gas chromatography methods for high-precision isotopic analysis of nanomole quantities of silicate nitrogen. *Chem. Geol.* **240**, 1-10.

Bebout, G.E., Agard, P., Kobayashi, K., Moriguti, T., Nakamura, E. (2013) Devolatiliza-tion history and trace element mobility in deeply subducted sedimentary rocks: evidence from Western Alps HP/UHP suites. *Chem. Geol.* **342**, 1–20.

Bebout, G.E., Lazzeri, K.E., Geiger, C.A. (2016) Pathways for nitrogen cycling in Earth's crust and upper mantle: A review and new results for microporous beryl and cordierite. *Amer. Mineral.* **101**, 7-24.

Bebout, G.E., Banerjee, N.R., Izawa, M.R.M., Kobayashi, K., Lazzeri, K., Ranieri, L.A. and Nakamura, E. (2018) Nitrogen concentrations and isotopic compositions of seafloor-altered terrestrial basaltic glass: Implications for astrobiology. *Astrobiology* **18**, 330-342.

Bigeleisen, J., Mayer, M. G. (1947) Calculation of equilibrium constants for isotopic exchange reactions. *J. Chem. Phys.* **15**, 261.

Broach, R.W., & Kirchner, R.M. (2011) Structures of the K^+ and NH_4^+ forms of Linde J. *Micropor Mesopor Mat.* **143**, 398-400.

Busigny, V., Cartigny, P., Philippot, P., Ader, M., Javoy, M. (2003a) Massive recycling of nitrogen and other fluid-mobile elements (K, Rb, Cs, H) in a cold slab environment: evidence from HP to UHP oceanic metasediments of the Schistes Lustrés nappe (western Alps, Europe). *Earth Planet. Sci. Lett.* **215**, 27–42.

Busigny, V., Cartigny, P., Philippot, P., Javoy, M. (2003b) Ammonium quantification in muscovite by infrared spectroscopy. *Chem. Geol.* **198**, 21-31.

Busigny, V., Cartigny, P., Philippot, P., Javoy, M. (2004) Quantitative analysis of ammonium in biotite using infrared spectroscopy. Amer. Mineral. 89, 1625-1630.

Busigny, V., Laverne, C., Bonifacie, M. (2005) Nitrogen content and isotopic composition of oceanic crust at a superfast spreading ridge: a profile in altered basalts from ODP Site 1256, Leg 206. *Geochem. Geophys. Geosyst.* **6**, Q12O01.

Busigny, V., Cartigny, P., Philippot, P. (2011) Nitrogen isotopes in ophiolitic metagabbros: a re-evaluation of modern nitrogen fluxes in subduction zones and implication for the early Earth atmosphere. *Geochim. Cosmochim. Acta* **75**, 7502–7521.

Cartigny, P. and Marty, B. (2013) Nitrogen isotopes and mantle geodynamics: The emergence of life and the atmosphere–crust–mantle connection. *Elements* **9**, 359-366. Geochim. Cosmochim. Acta 226, 182-191.

Cherin P., Hamilton W.C., Post B. (1967) Position and thermal parameters of oxygen atoms in sodium nitrate. *Acta Crystallogr.* **23**, 455-460.

Cococcioni M. and Gironcoli S. (2005) Linear response approach to the calculation of the effective interaction parameters in the LDA+U method. *Phys. Rev. B.* **71**, 035105.

Dalou, C., Hirschmann, M.M., Jacobsen, S.D., Le Losq, C. (2019a) Raman spectroscopy study of C-O-H-N speciation in reduced basaltic glasses: Implications for reduced planetary mantles. *Geochim. Cosmochim. Acta* **265**, 32-47.

Dalou, C., Füri, E., Deligny, C., Piani, L., Caumon, M.-C., Laumonie, M. (2019b) Redox control on nitrogen isotope fractionation during planetary core formation. *PNAS* **116**, 14485-14494.

Deng, Y., Li, Y., Li, L. (2018) Experimental investigation of nitrogen isotopic effects associated with ammonia degassing at 0–70 ºC. *Geochim. Cosmochim. Acta* **226**, 182-191.

Dobrzhinetskaya, L.F., Wirth, R., Yang, J.S., Hutcheon, I.D., Weber, P.K., Green, H.W. (2009) High-pressure highly reduced nitrides and oxides from chromitite of a Tibetan ophiolite. *PNAS* **106**, 19233-19238.

Dauphas, N., Roskosz, M., Alp, E.E., Golden, D.C., Sio, C.K., Tissot, F.L.H., Hu, M.Y., Zhao, J., Gao, L., Morris, R.V. (2012) A general moment NRIXS approach to the determination of equilibrium Fe isotopic fractionation factors: application to goethite and jarosite. *Geochim. Cosmochim. Acta* **94**, 254-275.

Freudenthal, T., Wagner, T., Wenzhöfer, F., Zabel, M., and Wefer, G. (2001) Early diagenesis of organic matter from sediments of the eastern subtropical Atlantic: Evidence from stable nitrogen and carbon isotopes. *Geochim. Cosmochim. Acta* **65**, 1795-1808.

Haendel, D., Mühle, K., Nitzsche, H.-M., Stiehl, G., Wand, U. (1986) Isotopic variations of the fixed nitrogen in metamorphic rocks. *Geochim. Cosmochim. Acta* **50**, 749–758.

Halama, R., Bebout, G.E., John, T., Schenk, V. (2010) Nitrogen recycling in subducted oceanic lithosphere: The record in high- and ultrahigh-pressure metabasaltic rocks. *Geochim. Cosmochim. Acta* **74**, 1636-1652.

Harlov, D., Andrut, M., and Melzer, S. (2001) Characterization of NH_4-phlogopite (NH_4) (Mg_3) [$AlSi_3O_{10}$] (OH)$_2$ and ND_4-phlogopite (ND_4) (Mg_3) [$AlSi_3O_{10}$] (OD)$_2$ using IR spectroscopy and Rietveld refinement of XRD spectra. *Phys. Chem. Miner.* **28**, 77-86.

Hanschmann, G. (1981) Berechnung von Isotopieeffekten auf quantenchemischer Grundlage am Beispiel sticksoffhaltiger Moleku¨ le. *ZfI-Mitt.* **41**, 19–39.

Herzberg, G. (1955) Infra-red and Raman spectra of polyatomic molecules. Van Nostrand, New York Higashi S (1982) Tobelite, a new ammonium dioctahedral mica. *Mineral. J.* **11**, 138-146.

Huang, F., Chen, L., Wu, Z., and Wang, W. (2013) First-principles calculations of equilibrium Mg isotope fractionations between garnet, clinopyroxene, orthopyroxene, and olivine: implications for Mg isotope thermometry. *Earth Planet. Sci. Lett.* **367**, 61-70.

Jo, J., Yamanaka, T., Kashimura, T., Okunishi, Y., Kuwahara, Y., Kadota, I., Miyoshi, Y., Ishibashi, J. & Chiba H. (2018) Mineral nitrogen isotope signature in clay minerals formed under high ammonium environment conditions in sediment associated with ammonium-rich sediment-hosted hydrothermal system. *Geochem. J.* **52**, 1-17.

Karamanos, R.E. and Rennie, D.A. (1978) Nitrogen isotope fractionation during ammonium exchange reactions with soil clay. *Can. J. Soil Sci.* **58**, 53-60.

Li, L., and Bebout, G.E. (2005) Carbon and nitrogen geochemistry of sediments in the Central American convergent margin: Insights regarding subduction input fluxes, diagenesis, and paleoproductivity. *J. Geophys. Res.* **110**, B11202. Doi: 10.1029/2004JB003276.

Li, L., Bebout, G.E., Idleman, B.D. (2007) Nitrogen concentration and $\delta^{15}N$ of altered oceanic crust obtained on ODP Legs 129 and 185: insights into alteration-related nitrogen enrichment and the nitrogen subduction budget. *Geochim. Cosmochim. Acta* **71**, 2344-2360.

Li, L., Cartigny, P., Ader, M. (2009) Kinetic nitrogen isotope fractionation associated with thermal decomposition of NH_3: experimental results and potential ap-

plications to trace the origin of N_2 in natural gas and hydrothermal systems. *Geochim. Cosmochim. Acta* **73**, 6282–6297.

Li, L., Sherwood Lollar, B., Li, H., Wortmann, U.G., Lacrampe-Couloume, G. (2012) Am-monium stability and nitrogen isotope fractionations for NH_4^+–$NH_{3(aq)}$–$NH_{3(gas)}$ systems at 20–70 ºC and pH of 2–13: applications to habitability and nitro-gen cycling in low-temperature hydrothermal systems. *Geochim. Cosmochim. Acta* **84**, 280–296.

Li, L., Zheng, Y.-F., Cartigny, P., Li, J. (2014) Anomalous nitrogen isotopes in ultrahigh-pressure metamorphic rocks from the Sulu orogenic belt: Effect of abiotic nitrogen reduction during fluid–rock interaction. *Earth Planet. Sci. Lett.* **403**, 67-78.

Li, L., He, Y., Zhang, Z., Liu, Y. (2021) Nitrogen isotope fractionations among gaseous and aqueous NH_4^+, NH_3, N_2 and metal-ammine complexes: Theoretical calculations and applications. *Geochim. Cosmochim. Acta*, Acceptance with minor typo revision.

Li, Y., Keppler, H. (2014) Nitrogen speciation in mantle and crustal fluids. *Geochim. Cosmochim. Acta* **129**, 13–32.

Li, Y., Wiedenbeck, M., Shcheka, S., Keppler, H. (2013) Nitrogen solubility in upper mantle minerals. *Earth Planet. Sci. Lett.* **377–378**, 311–323.

Li, Y., Marty, B., Shcheka, S., Keppler, H. (2016) Nitrogen isotope fractionation during terrestrial core-mantle separation. *Geochem. Perspect. Lett.* **2**, 138-147.

Li, K., Li, L., Pearson, D.G., Stachel, T. (2019a) Diamond isotope compositions indicate altered igneous oceanic crust dominates deep carbon recycling. *Earth Planet. Sci. Lett.* **516**, 190-201.

Li, Y.H., Wang, W., Huang, S., Wang, K. and Wu, Z. (2019b) First principles investigation of the concentration effect on equilibrium fractionation of K isotopes in feldspars. *Geochim. Cosmochim. Acta* **245**, 374–384.

Li, Y.H., Wang, W., Wu, Z. and Huang, S. (2019c) First-principles investigation of equilibrium K isotope fractionation among K-bearing minerals. *Geochim. Cosmochim. Acta* **264**, 30-42.

Liu, Q., Tossell, J.A., Liu, Y. (2011) On the proper use of the Bigeleisen–Mayer equation and corrections to it in the calculation of isotopic fractionation equilibrium constants. *Geochim. Cosmochim. Acta* **74**, 6965-6983.

Liu X., Qi Y., Zheng D., Zhou C., He L. and Huang F. (2018) Diffusion coefficients of Mg isotopes in $MgSiO_3$ and Mg_2SiO_4 melts calculated by first-principles molecular dynamics simulations. *Geochim. Cosmochim. Acta* **223**, 364–376

Méheut M., Lazzeri M., Balan E. and Mauri F. (2009) Structural control over equilibrium silicon and oxygen isotopic fractionation: a first-principles density-functional theory study. *Chem. Geol.* **258**, 28-37.

Mesto, E., Scordari, F., Lacalamita, M., & Schingaro, E. (2012) Tobelite and NH_4^+-rich muscovite single crystals from Ordovician Armorican sandstones (Brittany, France): Structure and crystal chemistry. *Amer. Mineral.* **97**, 1460-1468.

Mikhail, S. and Sverjensky, D.A. (2014) Nitrogen speciation in upper mantle fluids and the origin of Earth's nitrogen-rich atmosphere. *Nature Geosci.* **7**, 816-819.

Mikhail, S., Barry, P.H., Sverjensky, D.A. (2017) The relationship between mantle pH

and the deep nitrogen cycle. *Geochim. Cosmochim. Acta* **209**, 149-160.

Mingram, B., Bräuer, K. (2001) Ammonium concentration and nitrogen isotope composition in metasedimentary rocks from different tectonometamorphic units of the European Variscan Belt. *Geochim. Cosmochim. Acta* **65**, 273–287.

Mabrouk, K.B., Kauffmann, T.H., Aroui, H., & Fontana, M.D. (2013) Raman study of cation effect on sulfate vibration modes in solid state and in aqueous solutions. *J. Raman Spectrosc.* **44**, 1603-1608.

Marty, B. and Dauphas, N. (2003) The nitrogen record of crust-mantle interaction and mantle convection from Archean to present. *Earth Planet. Sci. Lett.* **206**, 397-410.

Mookherjee, M., Redfern, S.A., Swainson, I.P., & Harlov, D.E. (2004) Low-temperature behaviour of ammonium ion in buddingtonite $[N(D/H)_4AlSi_3O_8]$ from neutron powder diffraction. *Phys. Chem. Miner.* **31**, 643-649.

Nimmo, J.K., & Lucas, B.W. (1973) A neutron diffraction determination of the crystal structure of α-phase potassium nitrate at 25 degrees C and 100 degrees C. *J. Phys. C Solid State Phys.* **6**, 201-211.

Nowotny H., Heger G. (1983) Structure refinement of strontium nitrate, $Sr(NO_3)_2$, and barium nitrate, $Ba(NO_3)_2$. *Acta Crystallographica C.* **39**, 952-956.

Perdew, J.P., Burke, K. and Ernzerhof, M. (1996) Generalized Gradient Approximation Made Simple. *Phys. Rev. Lett.* **77**, 3865-3868.

Petts D., Chacko T., Stachel T., Stern R. and Heaman L. (2015) A nitrogen isotope fractionation factor between diamond and its parental fluid derived from detailed SIMS analysis of a gem diamond and theoretical calculations. *Chem. Geol.* **410**, 188–200.

Pinti, D.L., Hashizume, K., Sugihara, A., Massault, M., Philippot, P. (2009) Isotopic fractionation of nitrogen and carbon in Paleoarchean cherts from Pilbara craton, Western Australia: Origin of ^{15}N-depleted nitrogen. *Geochim. Cosmochim. Acta* **73**, 3819-3848.

Plessen, B., Harlov, D.E., Henry, D., Guidotti, C.V. (2010) Ammonium loss and nitrogen isotopic fractionation in biotite as a function of metamorphic grade in metapelites from western Maine, USA. *Geochim. Cosmochim. Acta* **74**, 4759–4771.

Roskosz, M., Mysen, B.O., Cody, G.D. (2006) Dual speciation of nitrogen in silicate melts at high pressure and temperature: an experimental study. *Geochim. Cosmochim. Acta* **70**, 2902–2918.

Rustad, J.R., Yin, Q.-Z. (2009) Iron isotope fractionation in the Earth's lower mantle. *Nature Geosci.* **2**, 514–518.

Sadofsky, S.J., Bebout, G.E. (2000) Ammonium partitioning and nitrogen-isotope fractionation among coexisting micas during high-temperature fluid-rock interactions: examples from the New England Appalachians. *Geochim. Cosmochim. Acta* **64**, 2835 – 2849.

Sano, Y., Takahat, N., Nishio, Y., Marty, B. (1998) Nitrogen recycling in subduction zones. *Geophys. Res. Lett.* **25**, 2289-2292.

Scalan, R. N. (1958) The isotopic composition, concentration, and chemical state of the nitrogen in igneous rocks. PhD thesis, Univ. Arkansas, Fayetteville.

Schauble, E. (2004) Applying Stable Isotope Fractionation Theory to New Systems. *Rev. Mineral. Geochem.* **55**, 65-111.

Schauble, E. A. (2011) First-principles estimates of equilibrium magnesium isotope fractionation in silicate, oxide, carbonate and hexaaquamagnesium (2+) crystals. *Geochim. Cosmochim. Acta* **75**, 844–869.

Schlemper, E.O., & Hamilton, W.C. (1966) Neutron-Diffraction Study of the Structures of Ferroelectric and Paraelectric Ammonium Sulfate. *J. Chem. Phys.* **44**, 4498-4509.

Shannon R. D. (1976) Revised effective ionic radii and systematic studies of interatomic distances in halides and chalcogenides. *Acta Crystallogr. A* **32**, 751-767.

Sidey, V. (2016) On the effective ionic radii for ammonium. *Acta Crystallogr. B Struct. Sci. Cryst. Eng. Mater.* **72**, 626-633.

Stefan-Kharicha, M., Kharicha, A., Mogeritsch, J., Wu, M., Ludwig, A. (2018) Review of Ammonium Chloride−Water Solution Properties. *J. Chem. Eng. Data*. 63, 3170-3183.

Togo, A. and Tanaka, I. (2015) First principles phonon calculations in materials science. *Scr. Mater.* **108**, 1–5.

Urey, H. C. (1947) The thermodynamic properties of isotopic substances. *J. Chem. Soc.* (London), 562–581.

Vainshtein, B.K. (1956) Refinement of the structure of the group NH_4 in the structure of ammonium chloride. *Trudy Instituta Kristallografii Akademiya Nauk SSSR* **12**, 18-24.

Wang, W., Qin, T., Zhou, C., Huang, S., Wu, Z. and Huang, F. (2017) Concentration effect on equilibrium fractionation of Mg-Ca isotopes in carbonate minerals: insights from first-principles calculations. *Geochim. Cosmochim. Acta* **208**, 185–197.

Wentzcovitch, R.M., Yu, Y.G. and Wu, Z. (2010) Thermodynamic Properties and Phase Relations in Mantle Minerals Investigated by First Principles Quasiharmonic Theory. *Rev. Mineral. Geochem.* **71**, 59–98.

Watenphul A., Wunder B., Wirth R., Heinrich W. (2010) Ammonium-bearing clinopyroxene: A potential nitrogen reservoir in the Earth's mantle. *Chem. Geol.* **270**, 240-248.

Williams, L.B., Ferrell, R.E., Hutcheon, I., Bakel, A.J., Walsh, M.M., and Frouse, H.R. (1995) Nitrogen isotope geochemistry of organic matter and minerals during diagenesis and hydrocarbon migration. *Geochim. Cosmochim. Acta* **59**, 765-779.

Young, E.D., Tonui, E., Manning, C.E., Schauble, E., Macris, C.A. (2009) Spinel–olivine magnesium isotope thermometry in the mantle and implications for the Mg isotopic composition of Earth. Earth Planet. Sci. Lett. 288, 524–533.

Figure captions

Fig. 1. The optimized crystal structures of minerals and aqueous ammonium. Different color represent different atoms.

Fig. 2. (A) The distribution probability (green) and coordination number (red) of H atom in distance to N atom in aqueous ammonium. (B) Statistics of the N-H bond lengths from 20 snapshots of $NH_4Cl \cdot (H_2O)_{32}$.

Fig. 3. Comparison of vibrational frequencies of the NH_4^+ cluster in minerals between our calculated results and experimental measurements. Linear fitting yielded a slope of 1.003, indicating high consistence between our calculation results and experimental data (see Table S4 for data).

Fig. 4. The predicted $10^3 ln\beta$ of nitrate and ammonium minerals from 200-3000 K (A) with enlarged view for nitrate minerals at around 300 K (B) and for ammonium minerals at around 575 K. Mineral abbreviations: Jd = jadeite; Di = diopside; Ab = albite; Mc = microcline; Budd = buddingtonite; Phl = phlogopite; Bt = biotite; Tbl = tobelite.

Fig. 5. Correlation between $10^3 ln\beta$ (at 300K) and the N-H bond length illustrate the control of bond length on nitrogen isotope fractionation in minerals. The data of some minerals with various nitrogen concentrations (reflected by the ammonium occupation number (see Table 1) cluster closely, indicating little concentration effect on the nitrogen isotope fractionations. Mineral abbreviations are the same as Figure 4.

Fig. 6. Equilibrium nitrogen fractionations ($10^3 ln\alpha$) between individual minerals and aqueous ammonium. (A) shows the low-temperature range of nitrate and ammonium salts; (B) shows the medium-high temperature range of silicate minerals. See Table 2 for the general equation describing these temperature-dependent nitrogen fractionations. Mineral abbreviations are the same as Fig. 4.
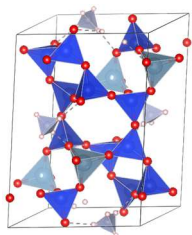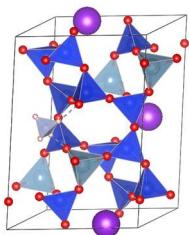
Buddingtonite   Microcline-(3KNH$_4$)   Microcline-(15KNH$_4$)   Albite-(3KNH$_4$)   Albite-(7KNH$_4$)
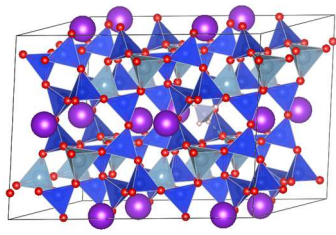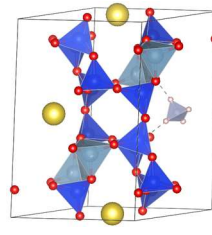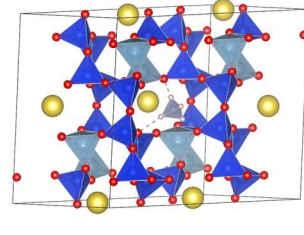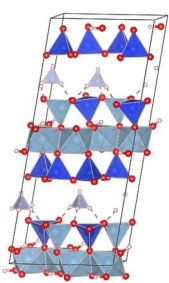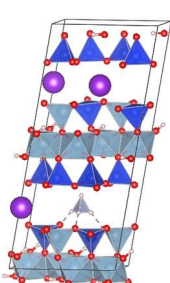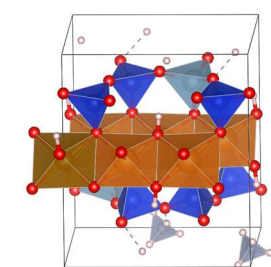
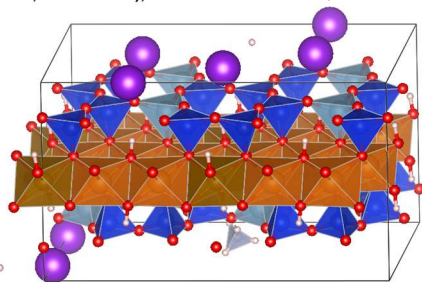Tobelite   Muscovite-(3KNH$_4$)   Muscovite-(7KNH$_4$)   Phlogopite-(NH$_4$)   Phlogopite-(3KNH$_4$)   Phlogopite-(7KNH$_4$)
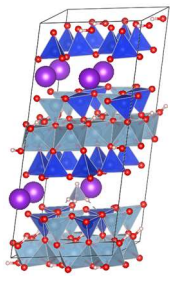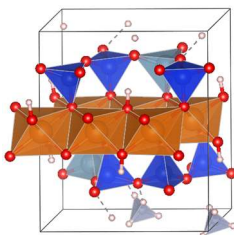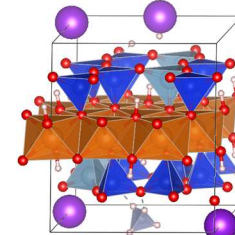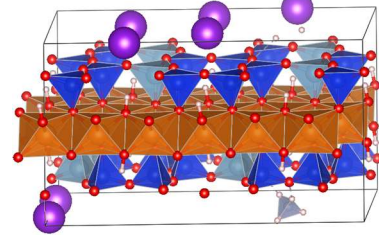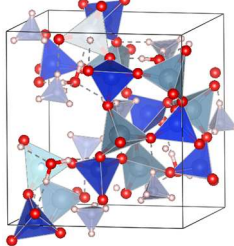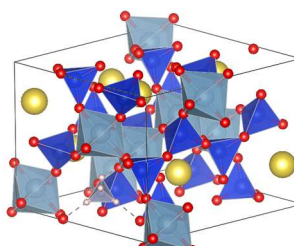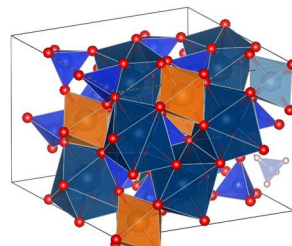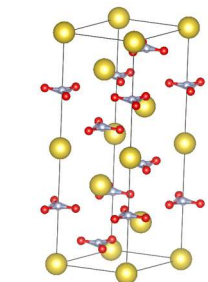
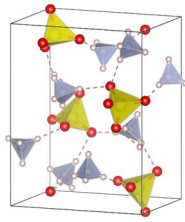Biotite-(NH$_4$)   Biotite-(7KNH$_4$)   Linde J   Jadeite-(7NaNH$_4$)   Diopside-(7CaNH$_4$)
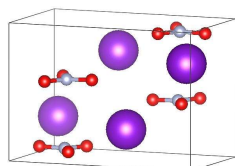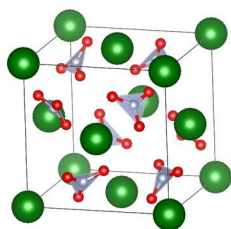
NaNO$_3$ KNO$_3$ BaNO$_3$ (NH$_4$)$_2$SO$_4$ NH$_4$NO$_3$-V   NH$_4$Cl
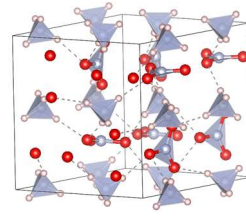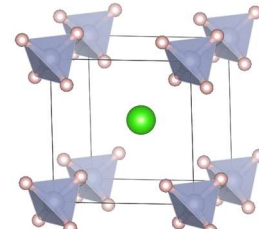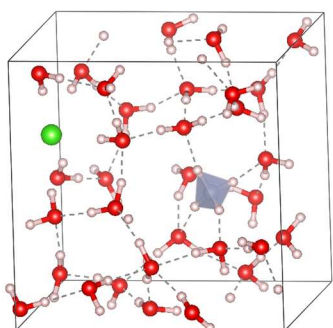
NH$_4$Cl·(H$_2$O)$_{32}$

Polyhedrons:
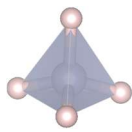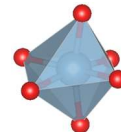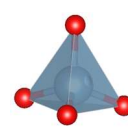
NH$_4$ MgO$_6$ AlO$_6$ AlO$_4$
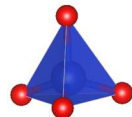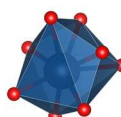
SiO$_4$ SO$_4$ CaO$_8$ FeO$_6$

Atoms:

H   Na   Cl   K   Ba

A

300 200 100 50 25 0 (°C)

$1000\ln\alpha_{Mineral-NH_4^+{}_{(aq)}}$ (‰)

50

40

30

20

10

0

- NaNO$_3$
- Ba(NO$_3$)$_2$
- KNO$_3$
- NH$_4$NO$_3$_NO$_3$
- NH$_4$NO$_3$_NH$_4$
- (NH$_4$)$_2$SO$_4$
- NH$_4$Cl

2.0   2.5   3.0   3.5

B

1000 700 500 400 300 200 (°C)

8

6

4

2

0

Jd

Di

Ab

Mc

Budd

Phl

Bt

Mus

Tbl

Clay

1.0   1.5   2.0

1000/T (/K)
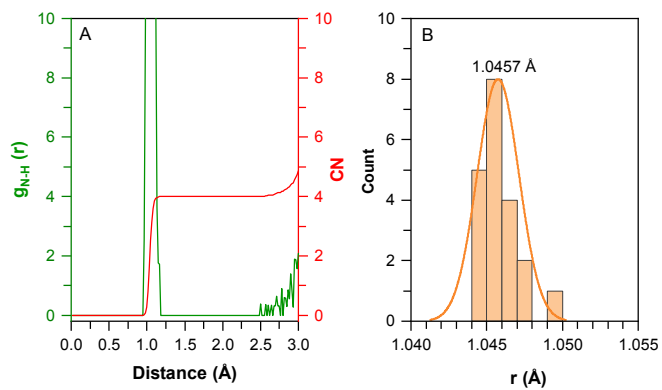
Table 1. The chemical formula, average bond lengths and polynomial fitting parameters of RPFR, $10^3\ln\beta = C_0 + C_1/10 \times x - C2/10^2 \times x^2 + C_3/10^3 \times x^3 - C_4/10^4 \times dx^4 + C_5/10^5 \times x^5 - C_6/10^6 \times x^6$, where x is $10^6/T^2$. Fitting temperature range is 200-3000 K.

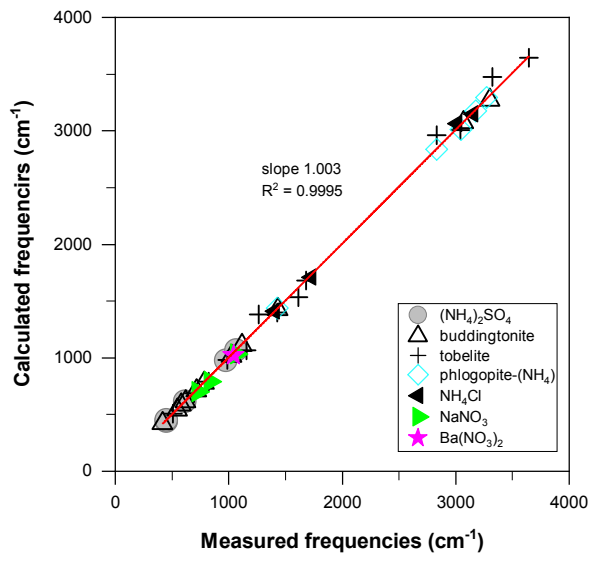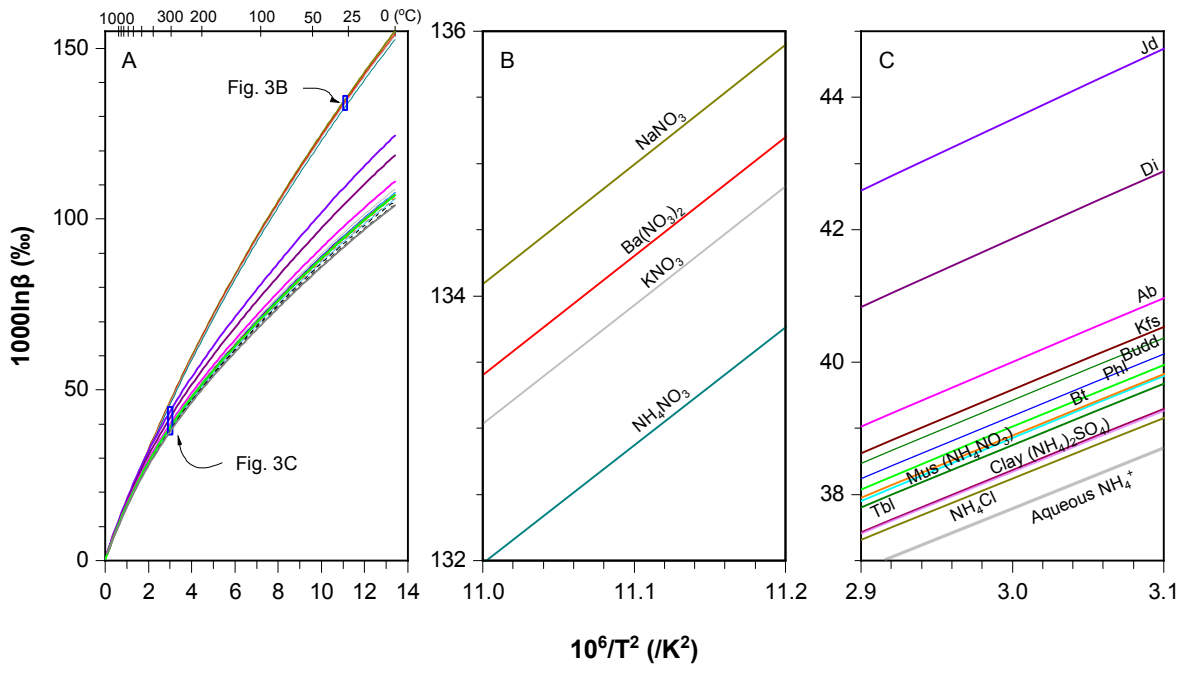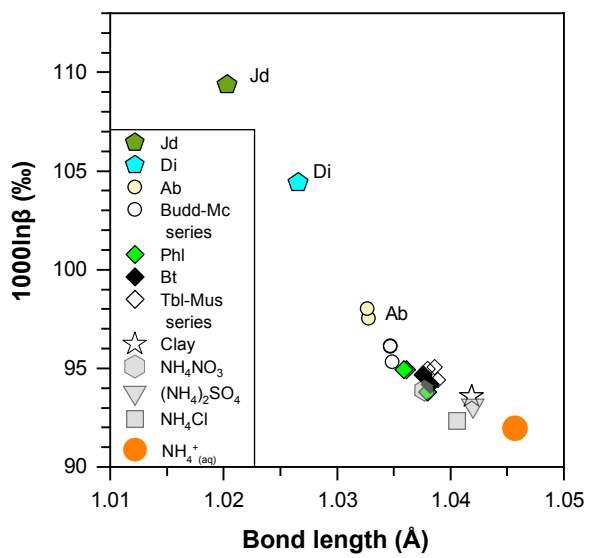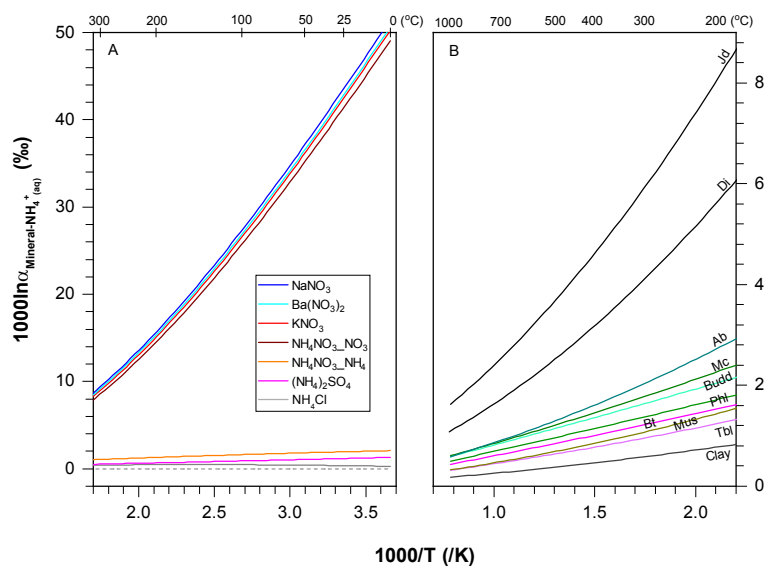| Minerals	$\dfrac{NH_4^+}{NH_4^+ + (K^+, Na^+, Ca^{2+})}$	Chemical formula	Bond length/Å	C_0	C_1	C_2	C_3	C_4	C_5	C_6
		N-O bond								
$NaNO_3$		$NaNO_3$	1.2733	0.01	177.46	88.893	55.818	25.523	6.7230	0.7440
$Ba(NO3)_2$		$Ba(NO3)_2$	1.2742	0.01	176.77	88.972	56.078	25.696	6.7762	0.7504
KNO_3		KNO_3	1.2761	0.01	175.71	87.311	54.499	24.837	6.5301	0.7219
NH_4NO_3 (V) - NO_3^-		NO_3^- in NH_4NO_3	1.2744	0.01	174.00	86.459	54.521	25.134	6.6705	0.7426
		N-H bond								
Jadeite	1/8	$(NH_4)Na_7Al_8Si_{16}O_{48}$	1.0203	0.47	197.73	249.14	282.60	180.25	57.719	7.2215
Diopside	1/8	$(NH_4)Ca_7Mg_7AlSi_{16}O_{48}$	1.0266	0.43	189.60	238.16	268.16	170.30	54.390	6.7936
Albite	1/4	$(NH_4)Na_3Al_4Si_{12}O_{32}$	1.0328	0.41	182.71	235.52	264.05	167.16	53.284	6.6472
	1/8	$(NH_4)Na_7Al_8Si_{24}O_{64}$	1.0327	0.41	182.77	234.53	262.86	166.39	53.034	6.6155
Buddingtonite-microcline	4/4	$(NH_4)AlSi_3O_8$	1.0349	0.41	181.39	237.14	265.72	168.15	53.591	6.6848
series	1/4	$(NH_4)K_3Al_4Si_{12}O_{32}$	1.0347	0.41	181.82	236.36	264.79	167.55	53.399	6.6606
	1/16	$(NH_4)K_{15}Al_{16}Si_{48}O_{128}$	1.0347	0.41	181.66	235.87	264.23	167.19	53.279	6.6455
Phlogopite	2/2	$(NH_4)Mg_3(Si_3Al)O_{10}(OH)$	1.0380	0.40	178.45	232.31	259.37	163.81	52.145	6.4994
	1/4	$(NH_4)K_3Mg_{12}(Si_3Al)_4O_{40}(OH)_4$	1.0361	0.41	180.06	234.27	262.11	165.74	52.798	6.5840
	1/8	$(NH_4)K_7Mg_{24}(Si_3Al)_8O_{80}(OH)_8$	1.0359	0.41	180.00	234.25	262.17	165.81	52.827	6.5881
Biotite	2/2	$(NH_4)_2FeMg_5(Si_3Al)_2O_{20}(OH)_2$	1.0382	0.40	179.37	233.92	261.38	165.14	52.582	6.5549
	1/8	$(NH_4)K_7Fe_4Mg_{20}(Si_3Al)_8O_{80}(OH)_8$	1.0376	0.40	179.00	231.80	258.84	163.50	52.054	6.4885
Tobelite-muscovite	4/4	$(NH_4)Al_3Si_3O_{10}(OH)_2$	1.0389	0.39	177.20	227.45	253.51	159.98	50.901	6.3424
series	1/4	$(NH_4)K_3Al_{12}Si_{12}O_{40}(OH)_8$	1.038	0.39	177.81	227.97	254.35	160.6	51.119	6.3709
	1/8	$(NH_4)K_7Al_{24}Si_{24}O_{80}(OH)_{16}$	1.0386	0.38	177.35	226.36	252.32	159.24	50.667	6.3133
Linde J		$(NH_4)_2(Si_2Al_2O_8)(H_2O)$	1.0419	0.36	175.15	222.95	247.08	155.41	49.347	6.1404
NH_4NO_3 (V) - NH_4^+		NH_4^+ in NH_4NO_3	1.0377	0.39	178.87	232.97	259.92	164.06	52.207	6.5055
$(NH_4)_2SO_4$		$(NH_4)_2SO_4$	1.042	0.36	175.43	224.56	248.78	156.40	49.645	6.1760
NH_4Cl		NH_4Cl	1.0406	0.37	175.61	227.24	252.31	158.86	50.476	6.2838
Aqueous NH_4^+		$NH_4Cl(H_2O)_{32}$	1.0457	0.34	172.48	218.82	241.27	151.28	47.943	5.9581

4 **Table 2.** Equilibrium nitrogen isotope fractionations between minerals and aqueous

5 ammonium, expressed in the general formulas $1000ln\alpha_{mineral-NH_4^+\ aqueous} = C_3 \times$

6 $(\frac{1000}{T})^3 + C_2 \times (\frac{1000}{T})^2 + C_1 \times \frac{1000}{T} + C_0$, in which T is temperature in Kelvin. The

7 fitting temperature range is 200-3000 K.

8

Mineral	C_3	C_2	C_1	C_0
NaNO$_3$	-0.7639	9.0105	-9.3307	2.29
Ba(NO3)$_2$	-0.7556	8.9138	-9.3038	2.28
KNO$_3$	-0.7531	8.9110	-9.4443	2.32
NH$_4$NO$_3$ (V) - NO$_3^-$	-0.7339	8.7685	-9.5183	2.35
Jadeite	-0.0363	1.2830	1.4111	-0.26
Diopside	-0.0196	0.9350	0.8649	-0.15
Albite	-0.0013	0.3209	0.7019	-0.16
Buddingtonite	-0.0030	0.0294	1.0037	-0.22
Microcline	-0.0025	0.1257	0.9150	-0.19
Phlogopite	-0.0007	0.0351	0.8258	-0.17
Biotite	-0.0013	0.0519	0.6915	-0.14
Tobelite	0.0024	0.0894	0.4235	-0.07
Muscovite	0.0048	0.1605	0.3492	-0.05
Clay	-0.0008	0.0896	0.1978	-0.03
NH$_4$NO$_3$ - NH$_4^+$	-0.0031	-0.0370	0.7941	-0.18
(NH$_4$)$_2$SO$_4$	-0.0005	0.0147	0.3303	-0.08
NH$_4$Cl	-0.0045	-0.0826	0.4681	-0.11

9